Effect of Heat Input on Microstructure, Residual Stress, and Corrosion Resistance of UNS 32101 Lean Duplex Stainless Steel Weld Joints

Naima Ouali, Khadidja Khenfer, Brahim Belkessa, Jamal Fajoui, Billel Cheniti, Brahim Idir, and Samuel Branchu

In the present work, the influence of heat input on phase balance, residual stresses and corrosion resistance of UNS 32101 lean duplex stainless steel welds has been investigated. Three weldment types were obtained with different heat inputs by varying welding current, using gas tungsten arc welding process. The results revealed that increasing heat input caused a significant microstructural evolution with high austenite fraction in weld metals. The residual stresses were measured on the surface and through the sample's thickness by x-ray diffraction technique based on $Sin^2\psi$ method. The results showed an inversely proportional relationship between the heat input and the compressive residual stresses on the surface and through the thickness of the weld metal. Potentiodynamic polarization tests of the different welded joints evaluated in 3.5% NaCl solution exhibited high corrosion resistance of the weld metal produced with the low heat input.

1. Introduction

Dual phase stainless steels (DSSs) are the most popular materials used, over the last 30 years, in oil and gas industry, pressure vessels and chemical transport, where high mechanical strength and excellent corrosion resistance are required (Ref 1). The microstructure of the DSS, that consists in ferrite and austenite phases in equal proportions, combines the attractive properties of ferritic and austenitic stainless steels: high tensile and fatigue strength, good weldability, high toughness and excellent resistance to pitting corrosion (Ref 1, 2). In order to reduce the high cost of DSS by reducing the alloying elements contents, lean duplex stainless steels (LDSSs) with less than 1.5% of Ni have been developed (Ref 3). Consequently, grades such as S30403 and S31603 as well as S32101 (LDX 2101) lower in cost than DSS were elaborated. The most popular is LDX 2101 that is increasingly used in steam generators and pressure vessels (Ref 4). This grade provides both superior mechanical strength and greater resistance to chloride stress corrosion cracking (Ref 5). The LDX 2101 has 21 wt.% chromium and fairly low nickel content of 1.5 wt.% and the composition is balanced with 5 wt.% of manganese and 0.22 wt.% of nitrogen to give rapid austenite formation in both the weld metal (WM) and in the heat affected zone (HAZ) (Ref 6). Furthermore, this grade with its superior strength allows thinner sections of LDSS to replace components made with thicker sections of standard austenitic stainless steels (Ref 7).

In fabrication industry, joining of metals is an important process where the main objective is to ensure an assembly with the same characteristics as the parent material, and that, by maintaining the mechanical properties and the corrosion resistance of the weld joint at the same level as the base metal. Several techniques have been used to join dissimilar materials. Bolting is an efficient technique for joining materials of different features that makes their welding process impossible. Urbikain et al. (Ref 8) developed a novel approach for joining dissimilar materials using friction drilling and form tapping that gave similar joints properties compared to conventional bolted joints with better corrosion resistance. On the other side, in stainless steel welding processes, consumables are usually over alloyed with nickel to ensure and promote the austenite reformation in the WM (Ref 5). Verma et al. (Ref 3), Muthupandi et al. (Ref 9) and Sadeghian et al. (Ref 10) mentioned that the best performance of the LDSS welds is obtained with an equal phase balance of austenite and ferrite and this ratio is dependent on various welding parameters, especially the heat input. It is known that during welding, the high heat input results in a slow cooling rate which allows a favorable phase balanced ratio. Yet, it causes grains coarsening, wider HAZ and the precipitation of brittle intermetallic phases (Ref 10). However, low heat input increases the amount of ferrite phase with the precipitation of CrN and Cr_2N phases which results in reduction in toughness and corrosion resistance (Ref 11). In order to guarantee an acceptable weld joint, a

Naima Ouali, Laboratory of Sciences and Materials Engineering, LSGM, FGMGP, University of Sciences and Technology, Houari Boumediene USTHB, BP 32 El Alia, 16111 Bab Ezzouar, Algiers, Algeria; and Research Center in Industrial Technologies, CRTI, P.O. Box 64, 16014 Cheraga, Algiers, Algeria; **Khadidja Khenfer**, Laboratory of Sciences and Materials Engineering, LSGM, FGMGP, University of Sciences and Technology, Houari Boumediene USTHB, BP 32 El Alia, 16111 Bab Ezzouar, Algiers, Algeria; **Brahim Belkessa, Billel Cheniti,** and **Brahim Idir**, Research Center in Industrial Technologies, CRTI, P.O. Box 64, 16014 Cheraga, Algiers, Algeria; and **Jamal Fajoui** and **Samuel Branchu**, E3M-GeM, Institut de recherche en Génie Civil et Mécanique (UMR CNRS 6183), IUT de Saint-Nazaire, 58 rue Michel Ange, BP 420, 44606 Saint-Nazaire Cedex, France. Contact e-mail: oualinaima@yahoo.fr.

ferrite/austenite phase balance is recommended, where this ratio is directly related to the heat input range (Ref 12, 13). Therefore, the choice of an adequate welding process, such as GTAW and Laser welding, is required to control the different welding conditions, especially the heat input and the cooling rate. It was reported (Ref 9, 14) that the fast cooling rate prevents the formation of deleterious precipitation, narrows the HAZ extent and reduces the residual stress level. Meanwhile, this cooling rate has to be slow enough to allow the formation of tolerable ratio of austenite phase.

During welding, the heat input generates localized expansion of the molten metal that is stopped by the base metal, which allows to some areas to cool faster than others. This phenomenon induces distortions and residual stresses in all the weld joint, where their level depends on several welding parameters. These RSs (compression and/or tensile stresses), that need to be controlled, affect both the mechanical performance and the corrosion resistance of all weld joint (Ref 12, 15). As reported by Ref 16, the tensile RSs have a detrimental effect on the welded structures where growth rate of defects is accelerated by increasing their magnitude.

Numerous research works investigated the effect of heat input on microstructural evolution and mechanical properties of austenitic stainless steels (ASS) weld joints. Unnikrishnan et al. (Ref 6) studied the effect of heat input on 304L ASS welds, and they found that the high heat input resulted in an increase in austenite grain size and compressive RSs with no precipitation occurrence. Kumar et al. (Ref 17) investigated the influence of three heat inputs on 304 ASS TIG welds. They found that the extent of grain coarsening in the HAZ was increased with the increase in the heat input. Alipooramirabada et al. (Ref 16) reported that, in multi-pass welds of high-strength low-alloy steel, the increase in heat input enlarged the WM and the HAZ extents and generated a low residual stress magnitude.

The corrosion behavior of LDX stainless steel joints depends mainly on the ferrite-austenite phase balance, that may be affected by the welding process, the selected welding parameters and the weld metal chemistry (Ref 11). Westin (Ref 13) and Brytan et al. (Ref 7) studied the influence of the welding parameters (heat input and composition of shielding gases) on the phase balance and corrosion resistance of LDX stainless steel TIG weld joints. They observed that the corrosion behavior can be improved by applying shielding gases rich in nitrogen or helium that increase the γ-phase content which is beneficial for corrosion resistance.

Nevertheless, to our knowledge, there are limited works in the literature dealing with the thermal conditions-properties relationship in LDSS welds, especially for multi-pass welding joints. Further, understanding of the heat input effect on the residual stresses, the microstructure and mechanical evolution and the corrosion resistance of the LDX 2101 welds is important, in order to optimize appropriate welding parameters. Therefore, the present work has been conducted to study the effect of the welding energy (heat input) on the microstructure of different zones and the hardness evolution through the LDX 2101 stainless steel GTAW weld joints. It aims, on the one hand, to determine the local RSs, by means of x-ray diffraction measurements, on the surface and through thickness of the weld joints and, on the other hand, to investigate the effect of the heat input on the pitting corrosion resistance of the weld metal.

2. Materials and Methods

The base material used in this work was a lean duplex stainless steel LDX 2101 (UNS S32101, EN 1.4162). The material was received in a plate form of 6.5 mm thickness and dimensions of 80×60 mm^2. A multi-pass (03 passes) welding process was employed to join the specimens using a duplex stainless steel filler metal (ER2209). The chemical compositions of base and filler metals are reported in Table 1. A single V-groove with included angle of 60° was performed with particular attention to remove impurities from the joint edges.

The welding operation was carried out using Gas Tungsten Arc Welding (GTAW) process with three (03) passes and pure argon (Ar. 99.99%) shielding gas at a constant flow of 10 L/min. The schematic illustration of the welded joint is shown in Fig. 1, whereas the welding parameters are summarized in Table 2.

During welding, the energy should be sufficient to prevent sticking, but not too large to prevent grain growth, which may induce a decrease in mechanical and corrosion properties. Three heat inputs were conducted according to the respective welding currents: 80, 100 and 130 A. The heat input was calculated as given in Eq 1 (Ref 18).

$$\text{Heat input} = \eta * \frac{I * U}{S * 1000} \quad \text{(kJ/mm)} \qquad \text{(Eq 1)}$$

where I is the welding current (A), U is the applied voltage (V), η is the welding thermal efficiency taken as 80% for the GTAW
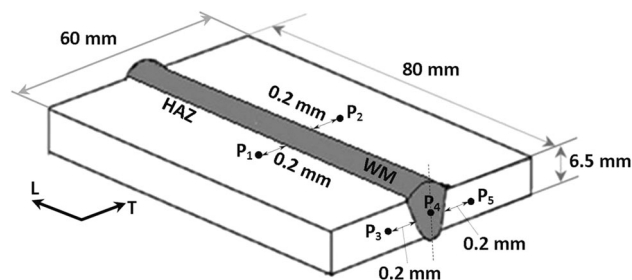

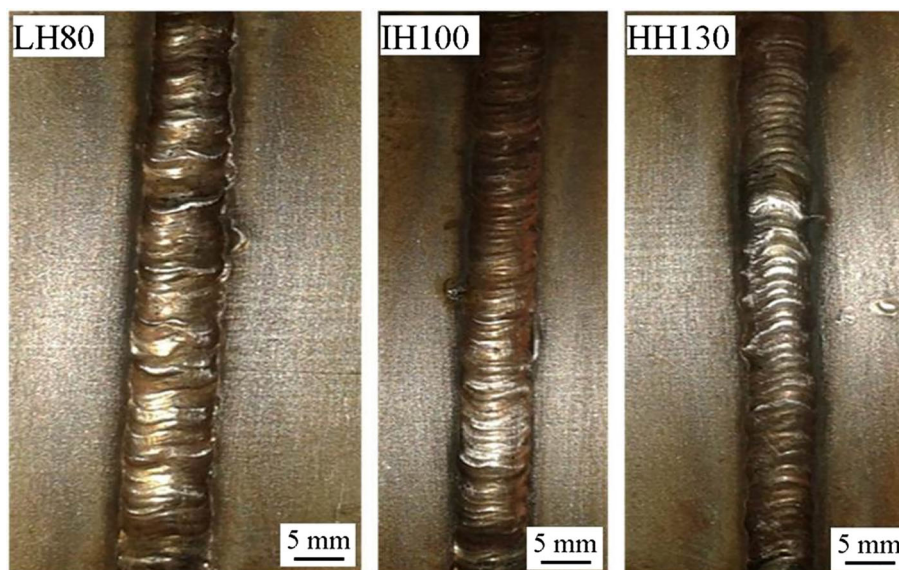**Fig. 1** Schematic illustration of the weld joint with residual stress measurements locations

Table 1 Chemical compositions of the base and filler metals (wt.%)

Alloy element	C	Mn	Si	Cr	Ni	P	S	Cu	Mo	N	Cr$_{eq}$/Ni$_{eq}$	PREN*
Base metal (S32101)	0.04	4.72	0.7	21.2	1.74	0.024	0.01	0.24	0.29	0.25	2.57	26.22
Filler metal (ER2209)	0.03	1.0	0.90	21.8	6.8	0.026	0.04	0.01	3.1	0.15	2.29	34.43
*Pitting resistance equivalent number												

Table 2 Parameters used during welding process

Specimen	Welding pass $n°$	Welding current, A	Welding voltage, V	Welding speed, mm/s	Average heat input per pass, kJ/mm	Average heat input, kJ/mm
LH80	1st	80	8.25	0.43	1.22	0.98
	2nd	80	8.25	0.54	0.97	
	3rd	80	8.75	0.72	0.77	
IH100	1st	100	9	0.54	1.33	1.05
	2nd	100	9.75	0.72	1.08	
	3rd	100	10.25	1.08	0.76	
HH130	1st	130	11.25	0.72	1.62	1.20
	2nd	130	11.75	1.08	1.13	
	3rd	130	12	1.44	0.86	

Fig. 2 Photographs of the as-welded conditions of LDX 2101 sheets with different heat inputs

process (Ref 17), and S is the welding speed (mm/s) measured manually.

In this paper, specimens were identified as LH80, IH100 and HH130, to refer to low heat input, intermediate heat input and high heat input, respectively, as shown in Fig. 2. In order to observe the microstructural evolution that occurs during welding process, metallographic sections transverse to the welding direction were prepared and etched with Beraha reagent (0.7 g $K_2S_2O_5$, 20 mL HCl, and 80 mL H_2O). The different weld regions were then analyzed using ZEISS optical microscope and Gemini 300 scanning electron microscope (SEM) with energy dispersive x-ray spectrometry analysis (EDS).

The ferrite and austenite volume fractions were estimated by automatic image analysis using a computer program attached to the optical microscope. Vickers's hardness profiles of the WM, HAZ and base metal (BM) were performed using Wolpert hardness tester under 10 kg/f. Three (03) measurement profiles were made in the middle of each joint and curves were plotted with the average values.

The residual stresses (RSs) were measured by x-ray diffraction, using a four-circle XRD 3003 PTS Seifert goniometer with Cr-Kα radiation as an x-ray source and k wave length of 2.289 Å. The generator voltage and current were 40 kV and 30 mA, respectively. The diffraction angle 2θ

ranges from 149° to 161°. The measurements were made on the {211} atomic plane of the studied material at $2\theta = 156.105°$. For each measurement, sixteen steps of (ψ) were employed, for positive and negative (ψ) tilts, between $-48°$ and $+45°$. The RS analysis was carried out based on the $\sin^2\psi$ method employed for polycrystalline materials (Ref 15, 19). The RS measurements were conducted on the as-welded surface samples (P_1, P_2) and through thickness on cut specimens (P_3, P_4 and P_5) as illustrated in Fig. 1. In order to target the HAZ, all the measurements were done at 0.2 mm from the fusion line, except for P_4, which was conducted on the middle of WM (see Fig. 1). Based on a linear regression fit, the variations of (2θ) versus ($\sin^2\psi$) plots were recorded and the RSs were evaluated.

The RS measurements were done in the longitudinal and transverse directions of the welding passes corresponding to $\varphi = 0°$ and $\varphi = 90°$, where φ is the rotation angle of the sample about its normal. The stresses were determined in the ferrite phase and identified by the displacement of the diffraction peaks of the ferrite that gives the sum of the macroscopic stresses (Order I) (Ref 12).

The corrosion behavior of the welded specimens was evaluated, on the one hand, by electrochemical impedance spectroscopy (EIS), to determine the electrical characteristics of the WMs and, on the other hand, by potentiodynamic

polarization tests. Electrochemical experiments were performed in a conventional three-electrode cell. The welded specimens were used alternately, as a working electrode (WE); a saturated calomel electrode and a platinum foil (surface area of 1.0 cm^2) were used as reference and counter electrode, respectively. EIS measurements were achieved at the open circuit potential for the frequency range of 100 kHz to 10 mHz, using a peak-to-peak voltage excitation of 10 mV. Z-view software was used to fit the EIS diagrams.

Potentiodynamic polarization tests were carried out at a scan rate of 1 mV/s. Before performing EIS diagrams and potentiodynamic polarization curves, the samples have been immersed in 3.5% NaCl solution at room temperature for 30 min until a steady state open circuit potential (E_{corr}) is reached. To confirm the accuracy of electrochemical measurements, the experiments were repeated at least three times, using Voltalab Radiometer Analytical instrument (PGZ301).

The Pitting Resistance Equivalent Number (PREN) was calculated according to the following formula (2) (Ref 20):

$$PREN = \%Cr + 3.3 \times (\%Mo) + 16 \times (\%N) \qquad (Eq\ 2)$$

The selective corrosion behavior of the austenite and ferrite phases of BM and WMs issued from 80 to 130 A heat input was examined by atomic force microscopy (AFM). The equipment employed is Bruker Icon ScanAsyst with Tapping mod using Nanosensor MESP-V2 probe at a constant force of 2.8 N/m and a resonant frequency of 75 kHz, the scan rate was 0.5 kHz, and the scanned surfaces were 5×5 μm^2 and 50×50 μm^2. Before the AFM analysis, the samples were polished using diamond paste to remove the surface oxide and ultrasonically cleaned in acetone. After that, the samples were electrolytically etched with 1 M KOH solution, applying 6 V of voltage for 8 s and immersed in 3.5% NaCl for 48 h.

3. Results and Discussion

3.1 Microstructural Analysis and Ferrite Content

Figure 3(a)-(c) illustrates transversal sections of the weldments obtained from the different heat inputs. It is observed that as the heat input increases, the WM width increases with full penetration; which agrees well with the results found by Unnikrishnan et al. (Ref 6) and Kumar et al. (Ref 17) A typical two-phase banded structure of the LDX 2101 BM with proportions of 52% ferrite and 48% austenite is shown in Fig. 4. The austenite phase (γ) is appeared as discontinuous light region, while the dark one is the ferrite phase (δ) with continuous morphology. Generally, the DSSs weld solidified in fully ferritic mode, while the austenite nucleated below the ferritic solvus temperature (Ref 18). It is found in the present investigation that the solidification mode is effectively fully ferritic since the Cr_{eq}/Ni_{eq} ratio is greater than 1.95 (Ref 3) (see Table 1). The Cr_{eq} and Ni_{eq} are calculated using Eq 3 and 4 (Ref 15).

$$Cr_{eq} = Cr + Mo + 0.7Nb \qquad (Eq\ 3)$$

$$Ni_{eq} = Ni + 35C + 20N + 0.25Cu \qquad (Eq\ 4)$$

Figure 5(a)-(f) shows the microstructural aspect of the LDX 2101 WM, fusion boundary and HAZ of the different heat inputs. It reveals a typical microstructure of DSSs weld that consists of δ-ferrite phase and reformed γ-austenite phase, where the WM contains more austenite than the HAZ and BM. In the WMs issued from LH80, IH100 and HH130 (Fig. 5a, b and c, respectively), the predominantly austenite γ-phase is appeared with different morphologies, such as grain boundary austenite (GBA), intragranular austenite (IGA) and Wid-
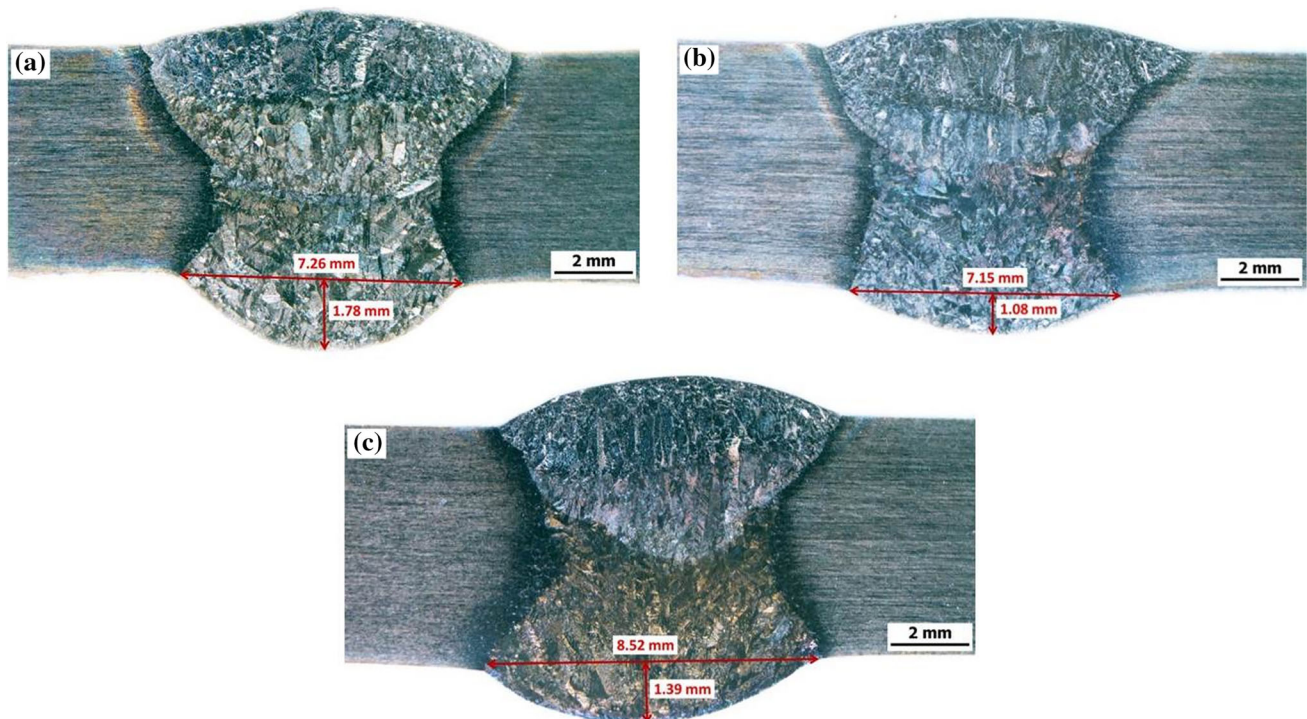

Fig. 3 Macrographs of the weld joints cross sections with different heat inputs: (a) LH 80, (b) IH 100 and (c) HH 130

manstätten austenite (WA) (Fig. 6), as confirmed by Ref 3, 4, 9. At first, the GBA phase nucleates from ferrite matrix, followed by the Widmanstätten secondary austenite formation along the δ-ferrite boundaries that grows into the ferritic grains. The IGA appears inside the ferrite grains as a consequence of sufficient cooling time (Ref 3, 11). This reformed austenite is transformed from the metastable ferrite phase during the reheating of subsequent weld passes. It is important to note that the arc energy should be sufficient to provide reasonable austenite formation in the WM and the HAZ. The minimum austenite content should be 30% (in last and root pass), in order to get an acceptable weld joint with good mechanical properties and high corrosion resistance (Ref 13). The results given in Table 3 indicate that the amount of austenite increases as the heat input increases. This phenomenon can be explained by the extending

of cooling time, that is more important with high heat input, which allows the transformation of δ-ferrite to γ-austenite. Hence, the diffusion of γ-stabilizing elements (Ni, N and Mo) is
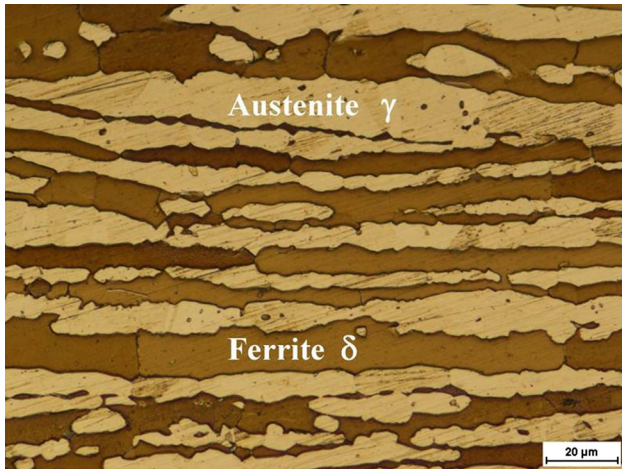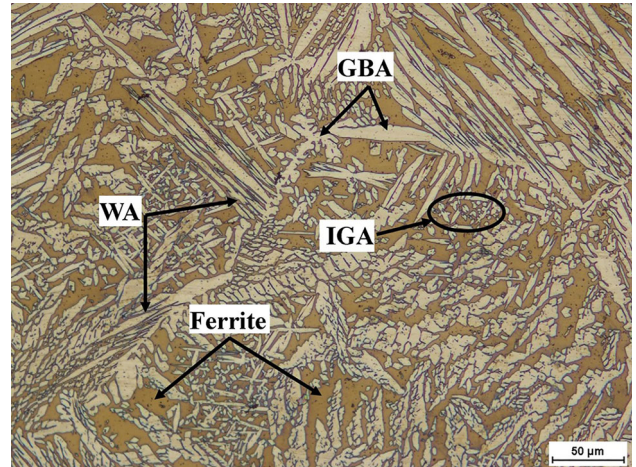

Fig. 6 Typical microstructure of the WM with different austenite morphologies: grain boundary austenite (GBA), Widmanstätten austenite (WA) and intragranular austenite (IGA)

Table 3 The measured ferrite-austenite contents using image analysis

Phase, %	Base metal	LH 80		IH 100		HH130	
		WM	HAZ	WM	HAZ	WM	HAZ
Ferrite	52	54.4	53.3	44.84	63.33	36.33	64
Austenite	48	45.6	32.5	55.16	34.70	63.67	35.9

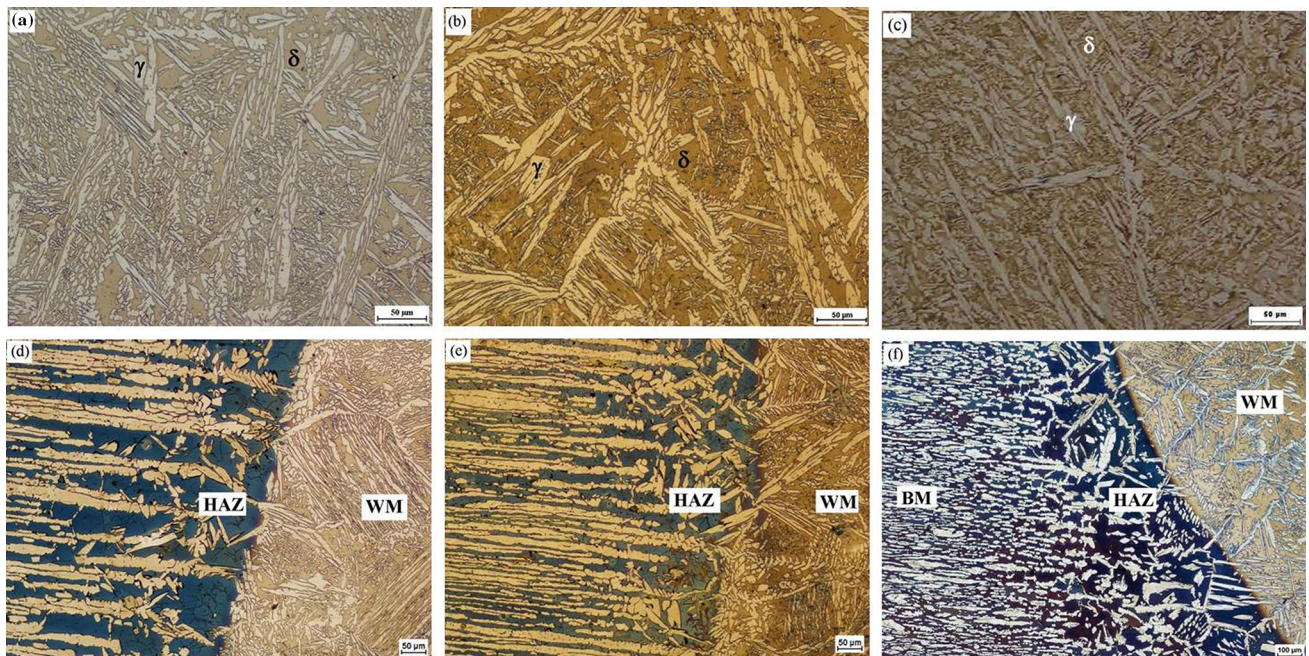**Fig. 4** Optical micrograph of LDX 2101 BM

Fig. 5 Optical micrographs of the weld metal (WM) and the heat affected zone (HAZ) issued from each heat input: (a) WM LH80, (b) WM IH100, (c) WM HH130, (d) HAZ LH80, (e) HAZ IH100 and (f) HAZ HH130

important and more γ-austenite is transformed. At low heat input (0.98 kJ/mm), the cooling rate is relatively high and results in short ferrite-austenite transformation time. However, at high heat input (1.20 kJ/mm), the cooling rate is slow and the WM is maintained at high temperature for long time which
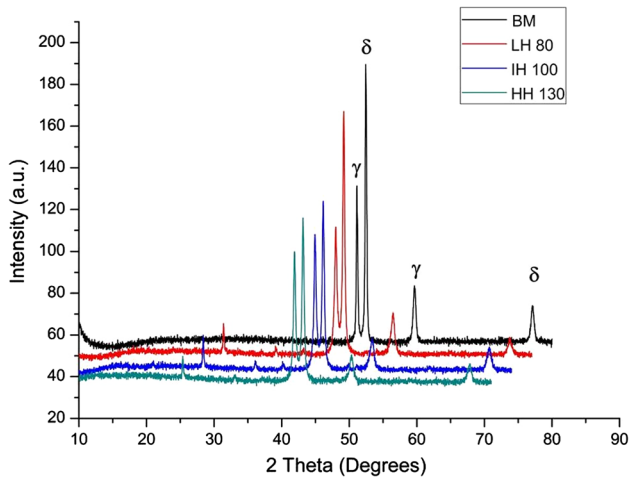

Fig. 7 XRD spectrum of LDX 2101 BM and WMs of different heat inputs

allows to more δ-ferrite transformation. These results are in agreement with those found by Ref 17, 21. The ferrite content measured in the different zones issued from each heat input is resumed in Table 3. It can be observed that in all WMs, the fraction of γ-austenite is higher than that of δ-ferrite; this can be attributed to the high Ni content in filler metal ER 2209 (6.8 wt.% Ni) and to the transformation time of δ-ferrite to austenite γ that increases with the heat input. On the other side, no precipitates or detrimental phases as σ phase or carbides are detected on the XRD spectrum of the WMs as shown in Fig. 7.

Figure 5(d)-(f) illustrates the microstructure of the HAZ corresponding to LH80, IH100 and HH130, respectively. It can be seen that with increasing the heat input, the microstructure exhibits an apparent change in grains morphology compared to BM. As shown in these figures, new coarse ferrite grains are developed accompanied with the formation of insufficient grains boundaries austenite (GBA) phase, with high ferrite content. These changes in microstructure compared to the BM are related to several parameters such as: the chemical composition, the welding parameters as well as the groove geometry (Ref 22, 23). It is worth noting that regardless of the heat input effect, the HAZ shows a narrow extent, which increases from 200 μm for LH80 to ∼ 284 μm for HH130, as illustrated by the SEM images in Fig. 8(a)-(c).

The EDS line-scan analyses shown in Fig. 9(a)-(c) are performed in order to observe the transition of elements across
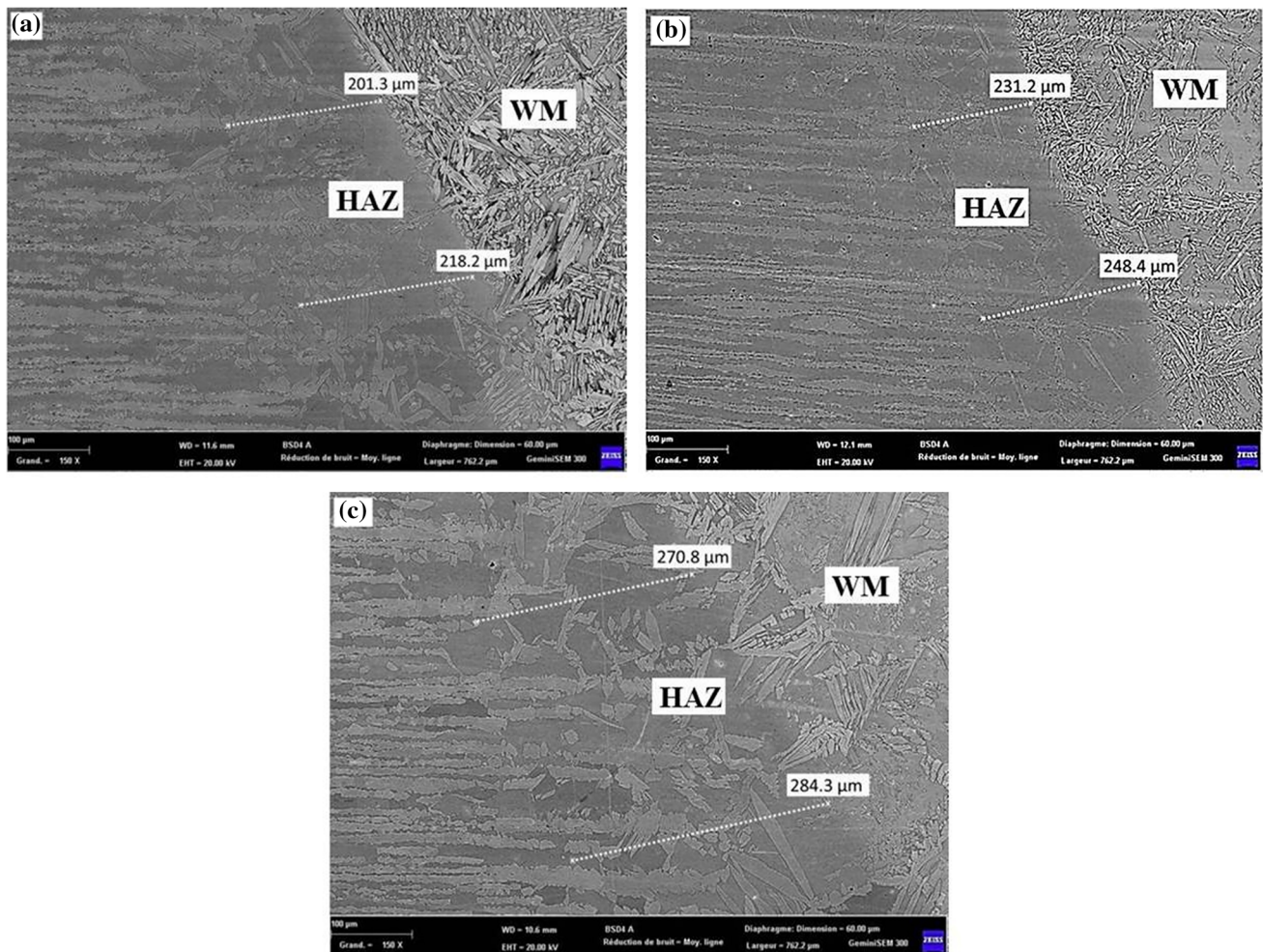

Fig. 8 SEM microstructure of the HAZ: (a) LH 80, (b) IH100 and (c) HH130
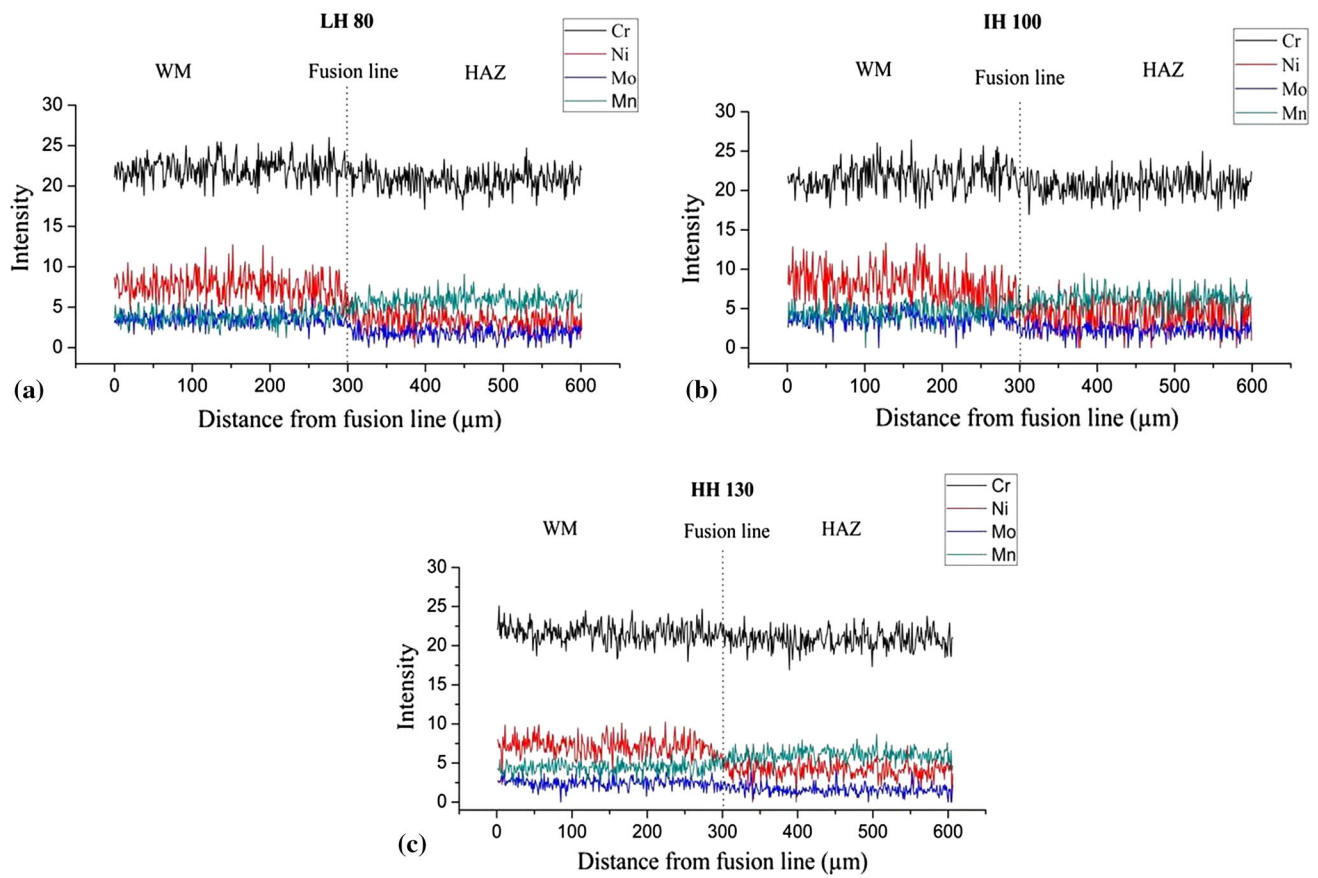
Fig. 9 EDS line-scan analysis of alloying elements within the joint across the WM/HAZ interface: (a) LH80, (b) IH100 and (c) HH130

Table 4 Chemical composition in WM and HAZ of different heat inputs (wt.%)

Sample	Zone	Cr	Ni	Mo	Mn
LH80	WM	22.06	6.83	2.19	1.98
	HAZ	20.88	1.69	…	4.29
IH100	WM	21.61	5.14	1.85	2.86
	HAZ	20.36	1.60	0.17	4.53
HH130	WM	21.60	5.92	1.59	2.58
	HAZ	20.45	1.71	0.48	4.48

Table 5 Distribution of longitudinal and transverse residual stresses on samples top surface

Sample	Location	σ_L, MPa	σ_T, MPa
LH80	P_1	− 276	− 165
	P_2	− 292	− 178
IH100	P_1	− 242	− 248
	P_2	− 251	− 152
HH130	P_1	− 226	− 166
	P_2	− 208	− 241

Table 6 Residual stresses in samples through the weld thickness

Sample	Location	σ_L, MPa	σ_T, MPa
LH80	P_3	− 53	− 195
	P_4	− 444	− 462
	P_5	− 74	− 225
IH100	P_3	− 150	− 210
	P_4	− 231	− 183
	P_5	− 254	− 462
HH130	P_3	− 186	− 213
	P_4	− 408	− 195
	P_5	− 266	− 124
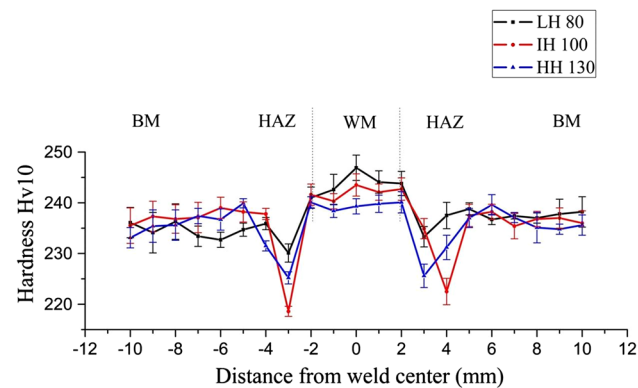
Fig. 10 Hardness profiles across the welded joints

Table 7 Fitting parameters of the impedance spectra of LDX 2101 BM and WMs in 3.5% NaCl solution at room temperature

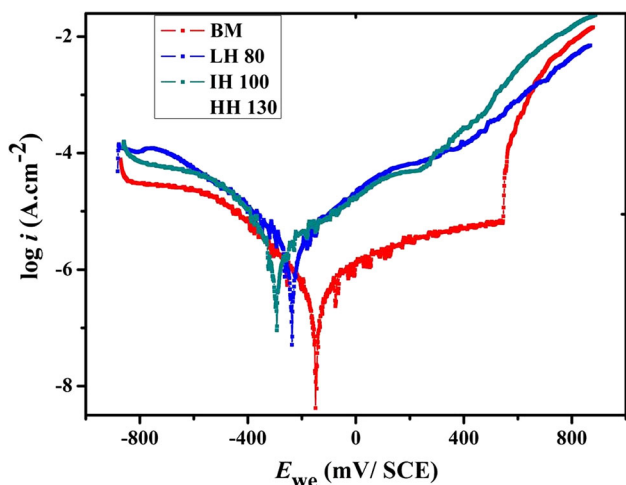| Samples	R_s, Ω cm^2	CPE$_1$, $\mu\Omega^{-1}$ S^n cm^{-2}	n_1	R_1, kΩ cm^2	CPE$_2$, $\mu\Omega^{-1}$ S^n cm^{-2}	n_2	R_2, kΩ cm^2	R_p, kΩ cm^2
BM	14	22.4	0.91	8.1	0.5	0.85	198	206.1
LH 80	11	20.7	0.94	10.9	19	0.97	109	119.2
IH100	18	23.8	0.95	6.4	69	0.96	11	17.4
HH 130	10	33.1	0.95	7.5	92	0.96	8	15.5

Fig. 11 Polarization curves of LDX 2101 BM and WMs in 3.5% NaCl solution at room temperature

the HAZ/WM interface. They revealed a concentration gradient of alloying elements (essentially; Ni, Mo and Mn) across the fusion line between the HAZ and WM. This phenomenon can be related to the difference in chemical composition between the BM and the filler metals, as mentioned in Table 1. Furthermore, it can be noticed that the heat input has a slight effect on the element activity across this interface. To get more information about the elements concentration, EDS point analysis has been conducted in both WM and HAZ issued from the different heat inputs (Table 4). The results show a uniform distribution of the alloying elements, where the chromium (Cr) content exhibits slight variation from WM to HAZ compared to Ni and Mn elements. The high concentration of Ni and Mn elements is attributed to the increase in austenite phase.

3.2 Hardness Variation

The effect of the heat input on the hardness distribution along the welded joints is shown in Fig. 10. It is observed that as the heat input increases, the hardness of the WM decreases (246.9, 243.5, and 239.3 HV corresponding to LH80, IH100 and HH130, respectively).

This slight decrease in the WM hardness from low to high heat input can be attributed to the difference in cooling rate and consequently the ferrite/austenite ratio. The increase in heat input results in the decrease in cooling rate, which promotes the γ-austenite formation and a decrease in δ-ferrite content in the WM (see Table 3), which leads to a decrease in hardness property (Ref 24). Noting that, the average hardness value of the LDX 2101 BM is found to be 240 HV and it decreases to

223 HV in the HAZ. This behavior is more probably due to the δ-ferrite grain coarsening, which decreases the mechanical properties of that region.

3.3 Residual Stress Evolution

The welding RSs can significantly affect the fatigue life and corrosion resistance of materials (Ref 6), and the heat input has a significant effect on their distribution on surface and through thickness as well (Ref 16). Table 5 shows the longitudinal and transverse RS values measured on both sides of the top surface of the welds (P$_1$ and P$_2$ in Fig. 1) for the different heat inputs. It can be seen that in all the heat inputs, the RSs are compressive in the longitudinal and transverse directions, and are not affected by the tempering of the subsequent weld pass. Furthermore, they are higher in the longitudinal direction than in the transverse one. This result is explained by the restrained and unrestrained cooling phenomena, which take different directions along the welding line (perpendicular and parallel). As reported in Table 5, the highest values of compressive RSs in longitudinal direction are obtained for low heat input at P$_2$ (about 292 MPa for LH80), and they decrease to 208 MPa with the increase in the heat input (HH130). These results are in good agreement with those found by Ref 16, 25.

Table 6 presents the RS values measured through thickness across the weld in three locations (P$_3$, P$_4$ and P$_5$ in Fig. 1). It can be seen that the stresses in the WM are directly affected by the heat input and are also compressive in both directions. The compressive nature of the RSs is related to the plastic deformation of the WM induced by its expansion after welding process. In this investigation, the RSs reach their maximum values in the middle of the WM (P$_4$), approximately 408 MPa for HH130 and 444 MPa for LH80. On the other side, there is a marked increase in longitudinal RS in the HAZ (P$_3$) and (P$_5$) as the heat input increases, where some transversal stress values become even larger than longitudinal ones. These measurements dispersion possibly results from the combined effect of machining and welding processes as motioned by Marques et al. (Ref 26) (Table 7).

3.4 Corrosion Behavior

Potentiodynamic polarization curves of BM and WMs issued from LH80, IH100 and HH130 are shown in Fig. 11. The corrosion current (I_{corr}), the corrosion potential (E_{corr}) and the polarization resistance (R_p) values of the different samples are summarized in Table 8. It can be observed that the lowest heat input results in the highest corrosion potential, where the LH80 WM exhibits a corrosion potential of about -147 mV versus SCE, which is clearly much higher and consequently nobler than the potentials observed for the WMs produced with IH100 and HH130 (-236 mV versus SCE and -292 mV

Table 8 Electrochemical corrosion parameters obtained from potentiodynamic polarization curves of various samples in 3.5% NaCl solution at room temperature

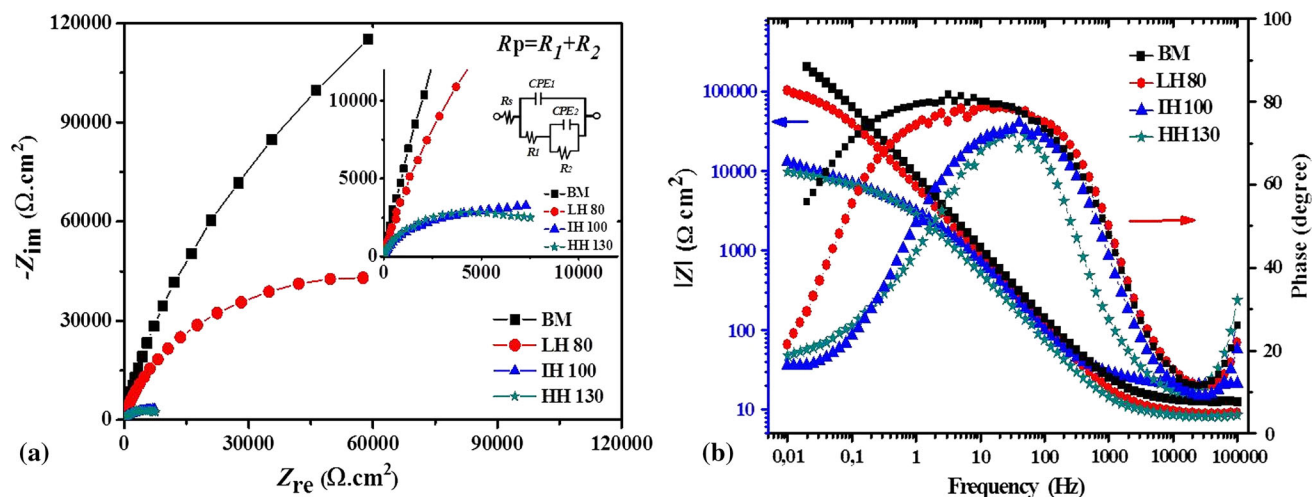| Samples	$E_{corr.}$, mV/SCE	$I_{corr.}$, μA cm^{-2}	β_a, V/dec	B_c, V/dec	R_p, kΩ cm^2
BM	− 229	0.26	0.52	0.14	187
LH 80	− 147	0.46	0.43	0.19	127
IH100	− 236	2.03	0.22	0.22	24.1
HH 130	− 292	2.21	0.18	0.31	22.8

Fig. 12 (a) Nyquist plots (inset: enlarged view) and (b) Bode magnitude and phase angle plots of LDX 2101 BM and WMs in 3.5% NaCl at room temperature

versus SCE, respectively). This behavior can be explained by the formation of a high content of secondary austenite (γ_2) with low concentrations of chromium, molybdenum as well as nitrogen, resulting in low pitting corrosion resistance (Ref 22).

The EIS experiments were carried out to confirm the data obtained by polarization. Figure 12(a)-(b) shows the Nyquist and Bode plots, respectively, obtained for each heat input sample in 3.5% NaCl at room temperature. The Nyquist diagram illustrated in Fig. 12(a) reveals that with increasing heat input the diameter of the capacitance semicircle decreases rapidly, indicating an increase in pitting corrosion rate. The equivalent circuit is shown in the inset of Fig. 12(a), where R_s is the solution resistance and R_1 is the charger transfer resistance. CPE_1 represents the capacitive behavior of the passive film, coupled with a resistance due to the ionic paths through the oxide film. CPE_2 represents the capacitive behavior of the double layer capacitance in the active areas and R_2 is the corresponding charge-transfer resistance. In all the bode plots, given the maxima of the phase angle is lower than 90°, constant phase element (CPE) was introduced to take into account the non-ideal electric behavior of the interface as shown in Fig. 12(b). This equivalent circuit is the most suitable to describe the pitting corrosion mechanism produced in the interface chloride/passive film/metal. Similar behavior was observed by Luo et al. (Ref 27) for 2205 duplex stainless steel in sodium thiosulphate solution.

The electrochemical impedance results of BM and WMs, shown in Table 8, demonstrate the great influence of the heat input on the corrosion kinetics. The BM has the highest corrosion resistance (206 kΩ cm^2), whereas the lowest corrosion resistance of about 15 kΩ cm^2 is associated with the WM with high heat input (HH 130). Both polarization curves and EIS data are in good agreement with each other, showing clearly that the WM produced with low heat input has better corrosion resistance than the one with intermediate and high heat input (IH 100 and HH 130), respectively.

Figure 13(a)-(c) illustrates the SEM images of the corrosion morphology of different surfaces after immersion in 3.5% NaCl for 48 h. It can be seen that the BM shows a smooth surface with few pits (Fig. 13a) compared to the WMs (Fig. 13b and c). The EDS analysis conducted in the pit area (Fig. 13d) shows that it is enriched of corrosion product with small amount of sulfur considered as the initiation site for pitting (Ref 28, 29) also and contains Cl, Na and high amount of O. Furthermore, the number of the pits becomes higher and their size deeper with increasing the heat input (Fig. 13b and c), causing a deep localized attack in the HH130 WM (Fig. 13c).

The 50 × 50 μm^2 surface topography of the BM, LH80 and HH130 WMs obtained by AFM are shown in Fig. 14(a)-(c), respectively. They revealed minor changes in the surface morphology of the BM with low value of roughness (196 nm) which may indicate a low corrosion activity over that surface. As soon as the heat input is increased, the sample surface
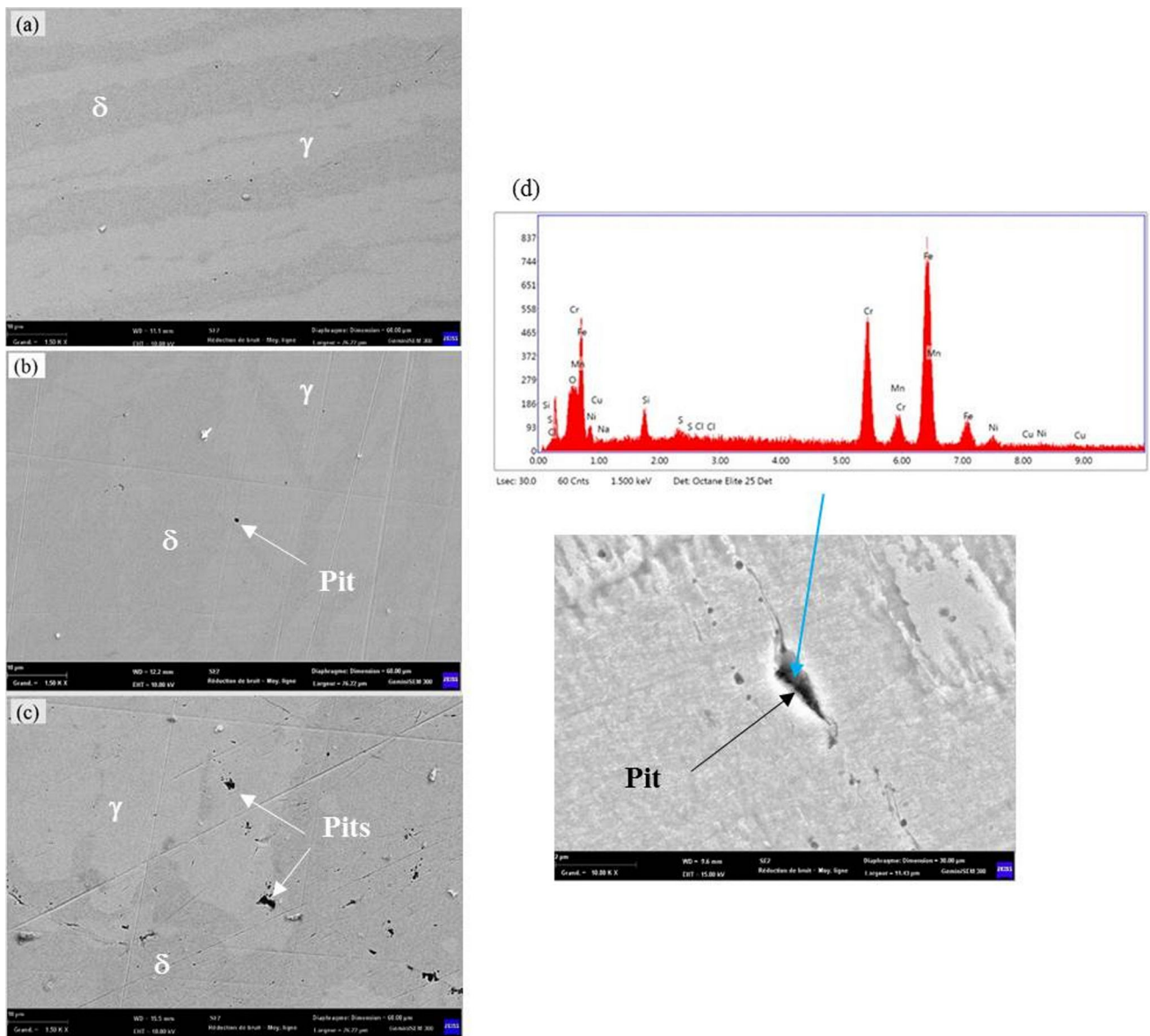
Fig. 13 SEM images of the corrosion morphology of different surfaces after immersion in 3.5% NaCl for 48 h: (a) BM, (b) LH80, (c) HH130 and (d) EDS analysis conducted in the pit area

changes and becomes rougher (264 and 448 nm for LH80 WM and HH130 WM, respectively). Figure 15(a) and (b) corresponds to the WM surfaces of LH80 and HH130, show clearly the nucleation of pits at δ/γ boundaries and their propagation almost exclusively in the ferrite region (selective dissolution). The literature reports several research works dealing with this selective dissolution (Ref 30-35). They pointed out that the weak pit potential of the δ phase and the nature of element present in each phase (δ and γ) especially Cr, Mo and N are the reason of this selective corrosion (Ref 36). On the other side, it can be seen that with increasing the heat input, the pits become more prominent, their size is larger (400-700 nm for 80 and 130 A, respectively), and they propagate deeply into the surface (30-60 nm for 80 and 130 A, respectively) as illustrated in the line profile shown in (Fig. 15c and d). This behavior can be related to the precipitation of secondary austenite (γ_2) at the surrounding of δ phase that becomes significant with increasing the heat input. This γ_2 that contains lower concentration of +

chromium element than that of primary austenite γ gives further preferential site for pitting attack (Ref 29, 37). Therefore, it can be said that the heat input has a direct influence on the pitting corrosion resistance of the weld joint.

4. Conclusion

From this work, the following conclusion can be drawn:

- Fully penetrated welds with no precipitation of carbides in the WMs and in the HAZ for the three heat inputs.
- A wide variety of microstructure resulting from both solidification and solid state transformation is induced by the GTAW process through the weld joint.
- Significant alteration of the ferrite-austenite phase balance in the HAZ and WM compared to the BM is observed
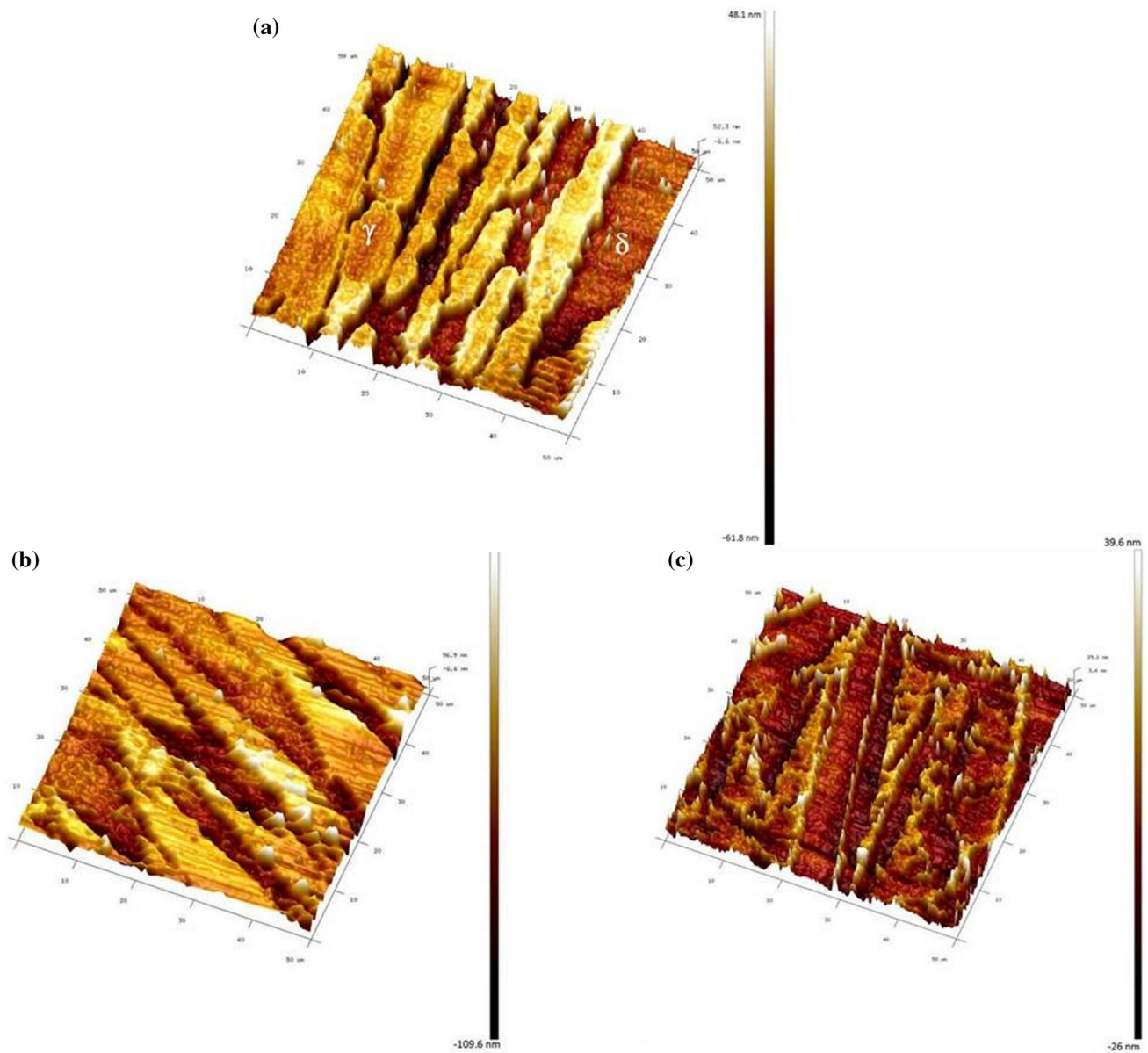
Fig. 14 AFM images of the 50 × 50 μm² corroded surfaces topography (a) BM, (b) WM LH80 and (c) WM HH130

with a high amount of δ ferrite in the HAZ. As the heat input increases, the ferrite content in the WM decreases.

- The increase in heat input causes a decrease in hardness in the WM which can be attributed to the difference in ferrite/austenite ratio.

- Heat input has a significant effect on welding residual stresses, the superficial residual stresses are compressive, and decrease as the heat input increases.

- Longitudinal and transverse RS measured through thickness of the weld joint are all compressive for each heat input.

- Pitting corrosion resistance of the LDX 2101 WMs decreases with increasing the heat input due to reformed secondary austenite with lower chromium, molybdenum and nitrogen content.

- Increasing the heat input, the pits are more prominent, their size is large, and they propagate deeply into the surface at δ/γ boundaries.

- The welding heat input has a direct influence on the residual stresses, through the microstructure (austenite/ferrite ratio) and the phase transformation, which affect the pitting corrosion resistance of the weld joint.
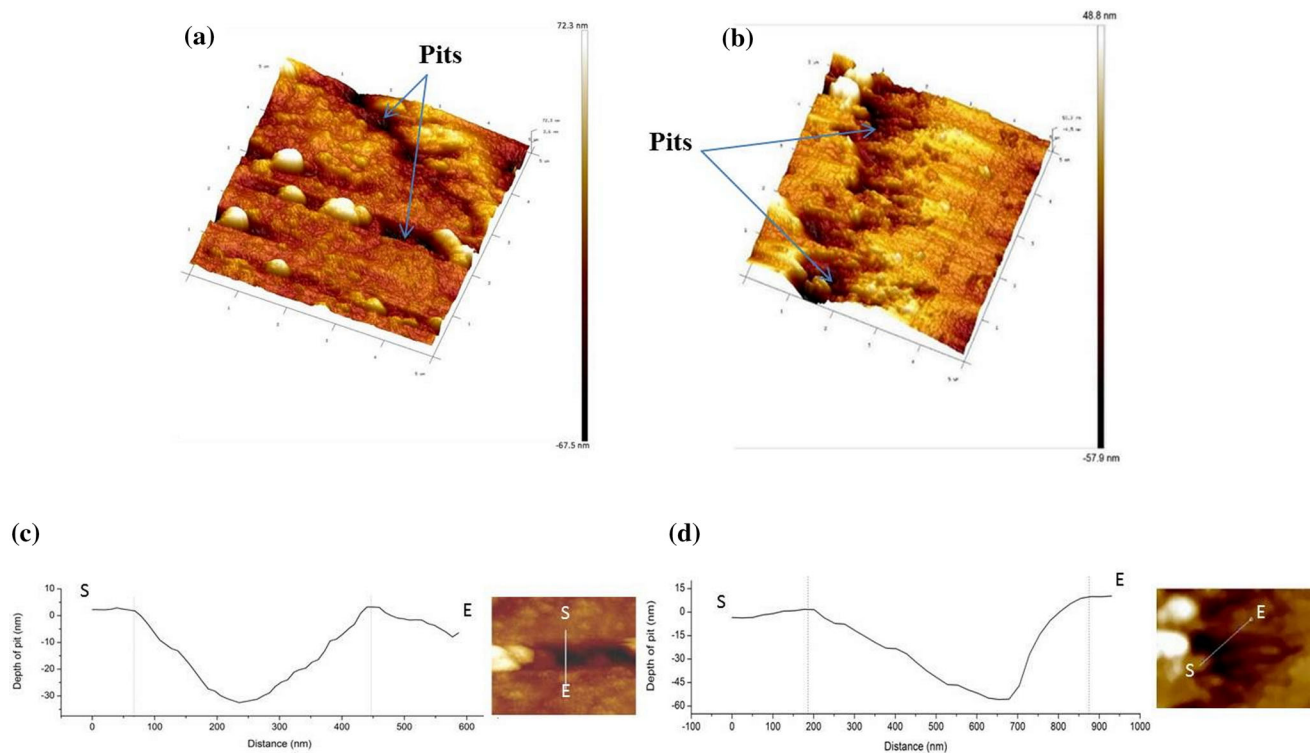
Fig. 15 AFM images of the 5 × 5 μm² corroded surfaces topography: (a) WM LH80, (b) WM HH130, (c) line profile of the pit area in LH 80 and (d) line profile of the pit area in HH 130

References

1. D.J.K. John and C. Lippold, *Welding Metallurgy and Weldability of Stainless Steels* (wiley, 2005)
2. R. Gunn, *Duplex Stainless Steels: Microstructure, Properties and Applications*, 1st edn. (Abington Publishing, 1997), p 219
3. J. Verma and R.V. Taiwade, Effect of Welding Processes and Conditions on the Microstructure, Mechanical Properties and Corrosion Resistance of Duplex Stainless Steel weldments—A Review, *J. Manuf. Process.*, 2017, **25**, p 134–152
4. Z. Brytan and J. Niagaj, Microstructural Characterization of Lean Duplex Stainless Steel UNS S32101 Welded Joints Using Electron Backscatter Diffraction, *Chiang Mai J. Sci.*, 2013, **40**(5), p 923–937
5. J. Pilhagen and R. Sandström, Influence of Nickel on the Toughness of Lean Duplex Stainless Steel Welds, *Mater. Sci. Eng., A*, 2014, **602**, p 49–57
6. R. Unnikrishnan, K.S.N.S. Idury, T.P. Ismail, A. Bhadauria, S.K. Shekhawat, R.K. Khatirkar, and S.G. Sapate, Effect of Heat Input on the Microstructure, Residual Stresses and Corrosion Resistance of 304L Austenitic Stainless Steel Weldments, *Mater. Charact.*, 2014, **93**, p 10–23
7. Z. Brytan, J. Niagaj, Ł. Reiman, Corrosion Studies Using Potentiodynamic and EIS Electrochemical Techniques of Welded Lean Duplex Stainless Steel UNS S82441, *Appl. Surf. Sci.*, 2016, **388**, p 160–168
8. G. Urbikain, J.M. Perez, L.N. Lo, and A. Andueza, Combination of Friction Drilling and Form Tapping Processes on Dissimilar Materials for Making Nutless Joints, *Proc. Inst. Mech. Eng. B J. Eng. Manuf.*, 2016, **232**(6), p 1–14
9. V. Muthupandi, P. Bala Srinivasan, S.K. Seshadri, and S. Sundaresan, Effect of Weld Metal Chemistry and Heat Input on the Structure and Properties of Duplex Stainless Steel Welds, *Mater. Sci. Eng., A*, 2003, **358**(1–2), p 9–16
10. M. Sadeghian, M. Shamanian, and A. Shafyei, Effect of Heat Input on Microstructure and Mechanical Properties of Dissimilar Joints between Super Duplex Stainless Steel and High Strength Low Alloy Steel, *Mater. Des.*, 2014, **60**, p 678–684
11. B. Alwin, A.K. Lakshminarayanan, M. Vasudevan, and P. Vasantharaja, Assessment of Stress Corrosion Cracking Resistance of Activated Tungsten Inert Gas-Welded Duplex Stainless Steel Joints, *J. Mater. Eng. Perform.*, 2017, **26**(12), p 5825–5836
12. Z. Brytan, J. Niagaj, W. Pakieła, and M. Bonek, FEM Modeling of Lean Duplex Stainless Steel Welding, *J. Achiev. Mater. Manuf. Eng.*, 2015, **70**(1), p 36–44
13. E.M. Westin, "Welds in the Lean Duplex Stainless Steel LDX 2101 Effect of Microstructure and Weld Oxides on Corrosion Properties Microstructure and Properties of Welds in the Lean Duplex Stainless Steel LDX 2101," Licentiate Thesis Thesis, Royal Inst, 2008
14. J. Pouquet, R.M. Miranda, L. Quintino, and S. Williams, Dissimilar Laser Welding of NiTi to Stainless Steel, *Int. J. Adv. Manuf. Technol.*, 2012, **61**, p 205–212
15. A. de Sousalins, L.F.G. de Souza, and M.C. Fonseca, Characterization of Mechanical Properties and Residual Stress in API, 5L X80 Steel Welded Joints, *J. Mater. Eng. Perform.*, 2017, **27**, p 124–137
16. H. Alipooramirabad, A. Paradowska, R. Ghomashchi, A. Kotousov, and M. Reid, Quantification of Residual Stresses in Multi-Pass Welds Using Neutron Diffraction, *J. Mater. Process. Technol.*, 2015, **226**, p 40–49
17. S. Kumar and A.S. Shahi, Effect of Heat Input on the Microstructure and Mechanical Properties of Gas Tungsten Arc Welded AISI, 304 Stainless Steel Joints, *Mater. Des.*, 2011, **32**(6), p 3617–3623
18. J. Verma, R.V. Taiwade, R.K. Khatirkar, S.G. Sapate, and A.D. Gaikwad, Microstructure, Mechanical and Intergranular Corrosion Behavior of Dissimilar DSS 2205 and ASS 316L Shielded Metal Arc Welds, *Trans. Indian Inst. Met.*, 2017, **70**(1), p 225–237

19. N. Syahida, M. Nasir, M. Khairul, A. Abdul, S. Mamat, and M. Iqbal, Review on Welding Residual Stress, *ARPN J. Eng. Appl. Sci.*, 2016, **11**(9), p 6166–6175

20. P. Bala Srinivasan, V. Muthupandi, W. Dietzel, and V. Sivan, Microstructure and Corrosion Behavior of Shielded Metal Arc-Welded Dissimilar Joints Comprising Duplex Stainless Steel and Low Alloy Steel, *J. Mater. Eng. Perform.*, 2006, **15**(6), p 758–764

21. Y. Yang, B. Yan, J. Li, and J. Wang, The Effect of Large Heat Input on the Microstructure and Corrosion Behaviour of Simulated Heat Affected Zone in 2205 Duplex Stainless Steel, *Corros. Sci.*, 2011, **53**(11), p 3756–3763

22. J. Nowacki and A. Lukojc, Microstructural Transformations of Heat Affected Zones in Duplex Steel Welded Joints, *Mater. Charact.*, 2006, **56**(4–5), p 436–441

23. Y.T. Shin, H.S. Shin, and H.W. Lee, Effects of Heat Input on Pitting Corrosion in Super Duplex Stainless Steel Weld Metals, *Met. Mater. Int.*, 2012, **18**(6), p 1037–1040

24. E. Mortazavi, R.A. Najafabadi, and A. Meysami, Effect of Heat Input on Microstructure and Mechanical Properties of Dissimilar Joints of AISI, 316L Steel and API, X70 High-Strength Low-Alloy Steel, *J. Iron. Steel Res. Int.*, 2017, **24**(12), p 1248–1253

25. W.C. Jiang, B.Y. Wang, J.M. Gong, and S.T. Tu, Finite Element Analysis of the Effect of Welding Heat Input and Layer Number on Residual Stress in Repair Welds for a Stainless Steel Clad Plate, *Mater. Des.*, 2011, **32**(5), p 2851–2857

26. M.J. Marques, A. Ramasamy, A.C. Batista, J.P. Nobre, and A. Loureiro, Effect of Heat Treatment on Microstructure and Residual Stress Fields of a Weld Multilayer Austenitic Steel Clad, *J. Mater. Process. Technol.*, 2015, **222**, p 52–60

27. H. Luo, C.F. Dong, K. Xiao, and X.G. Li, Characterization of Passive Film on 2205 Duplex Stainless Steel in Sodium Thiosulphate Solution, *Appl. Surf. Sci.*, 2011, **258**, p 631–639

28. A.J. Sedriks, Effects of Alloy Composition and Microstructure on the Passivity of Stainless Steels, *Corrosion*, 1986, **42**(7), p 376–389

29. Z. Cvijović and G. Radenković, Microstructure and Pitting Corrosion Resistance of Annealed Duplex Stainless Steel, *Corros. Sci.*, 2006, **48**(12), p 3887–3906

30. C. Park and H. Kwon, Effects of Aging at 475 C on Corrosion Properties of Tungsten-Containing Duplex Stainless Steels, *Corros. Sci.*, 2002, **44**, p 2817–2830

31. M.A. Baker, The Application of Surface Imaging Techniques to the Study of Pitting Corrosion Initiation in Stainless Steels, *Surf. Interface Anal.*, 1993, **20**, p 535–543

32. M. Femenia, J. Pan, C. Leygraf, and P. Luukkonen, In Situ Study of Selective Dissolution of Duplex Stainless Steel 2205 by Electrochemical Scanning Tunnelling Microscopy, *Corros. Sci.*, 2001, **43**, p 1939–1951

33. P.J. Antony, S. Chongdar, P. Kumar, and R. Raman, Corrosion of 2205 Duplex Stainless Steel in Chloride Medium Containing Sulfate-Reducing Bacteria, *Electrochim. Acta*, 2007, **52**, p 3985–3994

34. X.F. Yang and J.E. Castle, Using In Situ AFM to Investigate Corrosion and Passivation of Duplex Stainless Steels, *Surf. Interface Anal.*, 2002, **33**, p 894–899

35. K.H. Lo, C.T. Kwok, W.K. Chan, and D. Zeng, Corrosion Resistance of Duplex Stainless Steel Subjected to Long-Term Annealing in the Spinodal Decomposition Temperature Range, *Corros. Sci.*, 2012, **55**, p 267–271

36. R. Sriram and D. Tromans, Pitting Corrosion of Duplex Stainless Steels, *Corrosion*, 1989, **45**(10), p 804–810

37. C.H. Shek, C. Dong, J.K.L. Lai, and K.W. Wong, Early-Stage Widmanstätten Growth of the γ Phase in a Duplex Steel, *Metall. Mater. Trans. A Phys. Metall. Mater. Sci.*, 2000, **31**(1), p 15–19